

Paper III

Yongjia Song, Nils Gunnar Kvamstø, Shujie Ma (2007)

Estimates of poleward energy transport in experiments with a global atmospheric model with different horizontal resolution.

Estimates of poleward energy transport in experiments with a global atmospheric model with different horizontal resolution

Yongjia Song¹ Nils Gunnar Kvamstø^{1,2} Shujie Ma¹

1 Bjerknes Centre for Climate Research, University of Bergen, Norway

2 Geophysical Institute, University of Bergen, Norway

Abstract

This study presents estimates of the poleward energy transport based on the atmospheric daily reanalysis dataset of NCEP-DOE Reanalysis II from NOAA National Centers for Environmental Predictions and outputs from experiments with the atmospheric climate model ARPEGE with different horizontal resolution. The analysis focuses on the period from January 1979 to December 1990. The results show how the energy transport is represented in NCEP reanalyses and model experiments where the horizontal resolution is varying from T63 to T319, corresponding to a horizontal grid lengths from 2.8 to 0.5 degrees latitude. The results are showed in the annual and seasonal averages. The energy transport during the positive NAO events and negative NAO events is also investigated. The poleward total energy transport in the high resolution experiments has a better agreement with NCEP reanalysis data at mid and high latitudes than the low resolution experiment (T63). The same is also found for poleward dry static energy transport and latent heat transport components. The poleward total energy transport in the low resolution experiment is, however, closer to NCEP data in tropics. The energy transport by stationary eddies in the higher resolution experiments has a better agreements with NCEP data than the low resolution experiment. However, there are higher amplitudes of energy transport by transient eddies in the higher resolution experiments due stronger baroclinic activity at mid-latitudes.

1. Introduction

The ongoing warming trend in the Northern Hemisphere, which started around 1980, is noticeably increased in the Arctic region (Moritz et al., 2002). In agreement with the warming, an accelerated thinning of Arctic sea ice has taken place since the early 1990s (Holloway and Sou, 2002). The summer Arctic sea ice retreated particularly much in 2005, which was the second warmest year on record during the last half century. The climate changes taking place in Arctic might be caused by processes acting locally and/or by changes in heat transported to the area. Due to the effects of earth rotation and a non-uniform distribution of large-scale topography and heating sources/sinks in the northern Hemisphere, the transport of atmospheric energy toward Arctic varies from day to day, from month to month, seasonally and from year to year, while the earth-atmosphere system is approximately in a state of radiative energy balance from one year to the next (Vonder Haar and Oort, 1973). As we know, the climate system receives more energy from the sun than it emits to space in the tropics, while the case is opposite at high latitudes. To achieve the radiative balance of the earth-atmospheric system, circulations in the atmospheric and ocean transports lots of energy from tropics to polar regions. This poleward energy transport acts as an energy source for high latitudes and maintains the

observed atmospheric pole-equator temperature difference. This paper discusses the poleward energy transport in observational data and experiments with atmospheric climate models.

One method to evaluate the meridional heat transport was developed by Vonder Haar and Oort (1973) and adopted by Carissimo et al (1985), Masuda (1988), Kann et al. (1994) and others. With this method, the atmospheric poleward energy transport is calculated from meteorological variables, and the oceanic meridional heat transport is the residual term between the net radiation flux at the top of the atmosphere and the heat transport by the atmosphere. Estimates of the mean meridional energy transport by the ocean using this method, show large differences to those obtained using other approaches, such as the surface heat balance method (Hastenrath, 1982; Boer, 1986). This suggests that the oceanic heat transport using the residual method introduces some uncertainty (Holopainen and Fortelius, 1986), in the partition of meridional transport between atmosphere and ocean (Keith, 1995). However, it is clear that improvements in atmospheric heat transport estimates, resulting from better estimates of atmospheric states achieved from the use of modern data assimilation systems, reduces the uncertainties in the estimates of the ocean transports (Bengtsson and Shukla, 1988; Fortelius and Holopainen, 1990). It has also been demonstrated that the data assimilation system at ECMWF, including improved model parameterizations (e.g., diabatic initialization, deep and shallow convection), can improve the atmospheric energy transport significantly, particularly in the tropics (Wergen, 1988; Michaud and Derome 1991).

With the improved quality of satellite-derived radiation data, improved data assimilation systems and improved coupled climate models, Trenberth and Caron (2001) gave new estimates of the poleward energy transport. They pointed out that a much greater partition of the poleward transport is contributed by the atmosphere than by the ocean; the atmospheric transport accounts for 78% of the total in the northern Hemisphere and 92% in the southern Hemisphere. Earlier results based on experiments with atmospheric general circulation models (AGCMs) showed, however, large differences in the heat transport. For example, Stone and Risbey (1990) showed discrepancies as large as 40% in the total meridional energy transport between results from AGCMs and results based on observations. Further, the energy transport in NCAR's models CCM1 and CCM2 was about 20% larger than observations (Keith, 1995). Generally, it is vital to represent the energy variation well and keep energy conservation in AGCMs experiments. Studies show that one reason for differences between model estimates and observational estimates lies in the models ability to resolve mesoscale eddies. The coarse resolution normally used in AGCMs for climate experiments, are insufficient for detailed heat transport by synoptic scale systems (Masuda, 1988).

With higher resolution in AGCMs important additional information about mesoscale synoptic systems might be obtained. In addition, flows over topography will be better described. The basic idea of increasing the resolution is to transfer large-scale information onto smaller scales than normally has been resolved in climate models for climate change scenarios. There are three dynamical methods to improve the resolution of mesoscale weather systems in AGCMs. First, the most common way is use of a regional climate model of the atmosphere, where the lateral and surface boundary conditions are driven by a coarse resolution global model (Mcgregor, 1997; Giorgi and Mearns, 1999). Second, the stretched grid approach is used for downscaling of global

models with enhanced resolution for both prognostic fields and boundary forcing over the area of interest (Fox-Rabinovitz et al. 2001). Since the AGCM ARPEGE is used in this study, it is here necessary to mention that in the late 1980s the development of the stretched-grid spectral model was started at Météo-France (Courtier and Geleyn, 1988) using the approach developed by Schmidt (1977). The first regional climate simulation was performed with the ARPEGE global model in the mid-1990s (Deque and Piedelievre 1995). Lastly, a global AGCM with uniform high resolution might be used, where the surface conditions are often taken from global coupled integrations.

In this study, where the meridional heat transport is focused, only the last two methods of dynamical downscaling have been taken into account. Uncertainties in the downscaling process are difficult to quantify and evaluate (Murphy, 1999), therefore the knowledge of the meridional energy transport by the atmosphere might provide an indirect way of evaluating AGCMs. So in this paper, we intend to focus on the estimates of energy transport using the NCEP-DOE Reanalysis 2 dataset provided by NOAA National Center for Environmental Prediction and model outputs from four ARPEGE model experiments with different resolutions. The energy transport calculation used in this study is introduced in Section 2. The numerical model and the observational dataset is described 3, while we will devote attention to the results in section 4. Concluding remarks are given in section 5.

2. Atmospheric energy transport equations

a. Energy budget

Equations describing the energy transport of the atmosphere are derived from the equations of motion. An energy equation is first obtained from multiplication of the vector equation for horizontal motion by the horizontal wind (\mathbf{V}), and adding the thermodynamic equation and the moisture equation multiplied by the latent heat of condensation (L). Using the mass continuity equation we get the following form when integrating from bottom to the top of the atmosphere (Michaud and Derome, 1991):

$$\frac{\partial}{\partial t} \int_0^{P_s} (C_v T + \phi + Lq + V^2/2) dp / g + \int_0^{P_s} \nabla \cdot [(C_v T + \phi + Lq + V^2/2) \mathbf{V}] dp / g + \int_0^{P_s} \nabla \cdot (\mathbf{V} \phi) dp / g = Q_N$$

$$C_p T = C_v T + \phi$$

$$\frac{\partial}{\partial t} \int_0^{P_s} (C_p T + Lq + V^2/2) dp / g + \int_0^{P_s} \nabla \cdot [(C_p T + \phi + Lq + V^2/2) \mathbf{V}] dp / g = Q_N \quad (1)$$

In this study, the total atmospheric energy from the effective top of the atmosphere (P_0) to the surface (P_s) is defined as the vertical integration of total energy T_E , which is the sum of the internal energy I_E , potential energy P_E , latent energy L_E and kinetic energy K_E :

$$\begin{aligned}
I_E &= \int_0^{P_s} (C_p T) dp / g \\
P_E &= \int_0^{P_s} (\phi) dp / g \\
L_E &= \int_0^{P_s} (Lq) dp / g \\
K_E &= \int_0^{P_s} (V^2 / 2) dp / g \\
T_E &= \int_0^{P_s} (I_E + P_E + L_E + K_E) dp / g
\end{aligned} \tag{2}$$

Here C_p is the specific heat at constant pressure and L is the latent heat of vaporization. If we ignore the net heating rate Q_N , the total energy $T_E = I_E + P_E + L_E + K_E$ is conserved when integrated over the entire mass of the atmosphere. The net heating rate Q_N is the net downward radiation through the top-of-the-atmosphere plus a small contribution from thermal conduction to the ground. It may be written as follows:

$$Q_N = Q_1 - Q_2 - Q_f \tag{4}$$

We define

$$F_A = \int_0^{P_s} (I_E + P_E + L_E + K_E) \nabla dp / g$$

as the atmosphere energy transport. The dry static energy s is the sum of sensible heat $C_p T$ and potential energy ϕ , the moist static energy h is the sum of the dry static energy s and latent energy Lq , then F_A can be rewritten:

$$F_A = \int_0^{P_s} (h + k) \nabla dp / g \tag{5}$$

Replacing (1) with (2) (3) (4) and (5),

$$\frac{\partial}{\partial t} T_E + \nabla \cdot F_A = Q_1 - Q_2 - Q_f \tag{6}$$

Here Q_1 is the thermodynamic diabatic heating rate, and Q_2 is the column latent heating which equals $L(P - E)$. Q_f is the frictional heating arising from dissipation of kinetic energy. $\nabla \cdot F_A$ refers to divergence of energy transport which is linked to the energy source and sinks in the atmosphere.

b. Mass Correction

In fact, the analyses from observed wind data or four-dimensional assimilation systems do not generally satisfy the approximate condition of mass conservation (Gruber 1970; Masuda 1988), the transport calculation is affected by the small erroneous mass

flux divergence. The energy calculations are made after removal of spurious divergent horizontal mass fluxes, by subtracting the mean divergent wind from the horizontal wind, applied to the horizontal velocity vector at each available time at each atmospheric level (Boer, 1986; Masuda 1988; Kann et al. 1994). Here we follow Trenberth (1991) in including the pressure derivative term in the continuity equation, although its contribution turned out to be negligible in adjusting the velocity field by addition of an altitude independent constant to ensure that divergence of the vertically-integrated mass flux is zero.

$$\frac{\partial p_s}{\partial t} + \nabla \cdot \int_0^{P_s} \mathbf{V} dp - g(E - P) = \psi \quad (7)$$

Here we keep the term $g(E - P)$, which typically is ignored, but could contribute to energy budget errors of the order $\sim 10 \text{Wm}^{-2}$ (Trenberth 1997). The contribution of the term $\frac{\partial p_s}{\partial t}$ is also considered, which is around $\sim 5\%$ of the total. The mass correction minimizing the mass budget residual ψ , may be obtained by subtracting a barotropic correction V_c from V at each level.

$$\nabla^2 \chi = \psi$$

The Poisson's equation is solved on a sphere to give the potential of mass flux. The gradient of the potential function is divided by the total mass of the air column:

$$\begin{aligned} V_c &= \nabla \chi / (p_s - \int_0^{P_s} q dp / g) \\ V^c &= V - V_c \end{aligned} \quad (8)$$

Here V^c is the corrected velocity.

c. The characters of energy transport

The atmospheric motion can be divided into the contribution of a mean flow, stationary eddies and transient eddies by making use the method of time and zonal averaging. The mean meridional transport for any scalar X is then expressed as:

$$[\overline{Xv}] = [\overline{X}] [\overline{v}] + [\overline{X}^*] [\overline{v}^*] + [\overline{X'v'}] \quad (9)$$

Here X is a scalar field and v is the meridional velocity. Time mean and zonal average are denoted with an overbar and a bracket, primes and stars indicate deviations from time and zonal means respectively.

If the vertical integration is denoted as $\langle \rangle$, the meridional component of the total energy transport, $\langle (h+k)v \rangle$, is calculated at each horizontal gridpoint and integrated along each latitude circle. Thus the total transport across one latitude circle (ϕ) is:

$$PT_A = \int_0^{2\pi} a \cos \phi < (h+k)v > d\lambda \quad (10)$$

In this study the monthly means are computed before any vertical integration is performed. Trenberth et al. (2002) discuss differences that arise (up to order $\pm 10 \text{ W m}^{-2}$) in the divergence of total energy ($\nabla \cdot F_A$) if the vertical integral is performed at 6-hourly resolution. Then the monthly means were computed from the ERA-15 eta archive for January 1989.

3. The model and data

The ARPEGE/IFS (Action de Recherche Petit Echelle Grande Echelle / Integrated Forecast System) numerical model was developed as a community climate model in a joint effort between Meteo-France and European Centre for Medium range Weather Forecasts. ARPEGE is a spectral model with Fourier components along longitudes and Legendre polynoms along latitudes. The horizontal resolution for the dynamical fields is given with a triangular truncation in the spectral components (denoted T). The vertical resolution is given as a hybrid vertical coordinate, which means a weighting of sigma-coordinates and pressure-coordinates in such a way that the model surfaces follow the terrain at the ground (sigma-coordinates) and pressure surfaces at higher levels. In our experiments the default configuration of ARPEGE has been used with 31 vertical layers, 21 layers in the troposphere and 10 in the stratosphere. The spacing between the levels is most dense close to the ground with a vertical spacing of a few 100 meters near the ground. This spacing increases exponentially with height. The levels are expressed as $P(j) = a(j) \cdot P_s + b(j)$, here P_s is the surface pressure and $P(j)$ is the pressure at level j at any given grid point. a and b are the coefficients that defines the vertical levels. P_s is the surface pressure at a given grid cell.

Four experiments have been made using SST and distribution of sea-ice from GISST (Global Sea Ice and Sea Surface Temperature) reconstructed datasets. Integrations for around 13 years have been made, we keep the period from second year to the last year (from January 1979 to December 1990) to remove the influence of the initial condition. The following resolutions have been used: T63 which correspond to a horizontal grid length of 2.875 degrees, T159 which correspond to a grid length of 1.1 degrees and T319 which correspond to a grid length of 0.5 degrees. In addition we have made a similar experiment with stretched coordinates with resolution denoted T159S, where the number of horizontal grid points is the same as in T159, but where the grid resolution in Arctic is 0.5 degrees – similar to T319 - and reduced towards that of T42 over the Antarctica. A constant local stretching factor has been used defined as: $r = dx_j/dx_{j-1}$, where dx_j and dx_{j-1} are adjacent grid intervals and j is the horizontal index. In this way downscaling for Arctic is emphasized.

In this study we use scalar and vector harmonic analyses to solve the problems (Poisson equation, divergence of total energy, etc.) in spherical coordinates. The accuracy is uniform on the sphere and independent of the location of the poles. This fact eliminates a number of computational difficulties associated with solving partial differential equations on the sphere, including the accuracy and stability problems that can be created by clustering of grid points near the pole. Interpolation and smoothing on the sphere are

also significantly facilitated by harmonic analysis (Swarztrauber, 1979) between Gaussian and equally-spaced latitudinal grids.

The observational dataset used in this paper is NCEP-DOE Reanalysis II, and again, the four model experiments with different resolutions are T63, T159R, T159S and T319. The reason for choosing NCEP-DOE Reanalysis II instead of NCEP Reanalysis I is that an improved numerical model version has been used that reduces some known errors, mainly due to updates in the parameterizations schemes of physical processes, its temporal coverage with 4-times values a day from 1979/01/01 to 2005/12/01, coherent with our model experiment period. The spatial coverage is in a 2.5x2.5 degrees global grid (144x73) and 17 vertical levels which are 1000, 925, 850, 700, 600, 500, 400, 300, 250, 200, 150, 100, 70, 50, 30, 20, 10 hPa. To reduce computational costs etc., the daily data is used instead of data 4-times per day. Because of the time correlation that exists between synoptic observations, the daily sampling period is adequate, in fact, for a given computational effort. It is thus preferable to use a longer time series and a longer sampling interval since highly correlated data do not add much information to the estimate of time means (Michaud and Derome, 1991). The systematic error introduced by the interpolation to pressure levels implies that it would be most useful for transport calculations if results were saved daily in model coordinates. The physical fields used to compute energy transport are horizontal wind components (U, V) at all levels, temperature (T), geopotential height (Z), relative humidity and surface pressure Ps. The downward solar radiation flux, the upward solar radiation flux and the upward longwave radiation flux on top of atmosphere are used to calculate the net downward radiation through the top-of-the-atmosphere and further to get an estimate of the net upward surface flux Fs and Ocean energy transport. The humidity is converted to specific humidity (Q) before computation energy transport, using the following equations (Bolton 1980):

$$\begin{aligned} e_s &= 6.112 * \exp((17.67 * T)/(T + 243.5)); \\ e &= e_s * (RH/100.0); \\ Q &= (0.622 * e)/(p - (0.378 * e)), \end{aligned}$$

where T is temperature in deg C, e_s is saturation vapor pressure in hPa, e is vapor pressure in hPa, RH is Relative Humidity in percent, p is surface pressure in hPa, Q is specific humidity in kg/kg.

In model results all the final output fields are on the 16 vertical levels (using the postprocessor of ARPEGE model) which are 10, 30, 50, 70, 100, 150, 200, 250, 300, 400, 500, 600, 700, 850, 925, 1000 hPa. There is no 20 hPa level compared with NCEP Reanalysis 2 data. The model output data, horizontal wind components, the temperature, the geopotential height and the specific humidity at all 16 levels are used to calculate the energy transport directly, however, the surface pressure (Ps) need be derived from following equations:

$$\begin{aligned} \ln(P_s/P_1) &= \ln(P_2/P_1)[(Z_s-Z_1)/(Z_2-Z_1)] & Z_s > Z \text{ at } 1000 \text{ hPa} \\ P_s &= P_{1000} \exp[(Z_{1000}-Z_s)G_0/(RT_v)] & Z_s < Z \text{ at } 1000 \text{ hPa} \end{aligned}$$

where P_s is the surface pressure, Z_2 and Z_1 are the geopotential heights at the standard pressure surfaces immediately above and below Z_s , and P_2 and P_1 are the corresponding

pressure levels. R is the gas constant, G_0 is the geopotential gravity constant, Z_{1000} is the 1000 hPa geopotential height, and P_{1000} is the 1000 hPa pressure, and T_v is the virtual temperature at 1000 hPa, given by $T_v = T_{1000}(1 + 0.61Q_{1000})$ and Q_{1000} is the 1000 hPa specific humidity. For the present calculation it was assumed that there was no difference between the geometric height Z_s of the surface and the geopotential height Z .

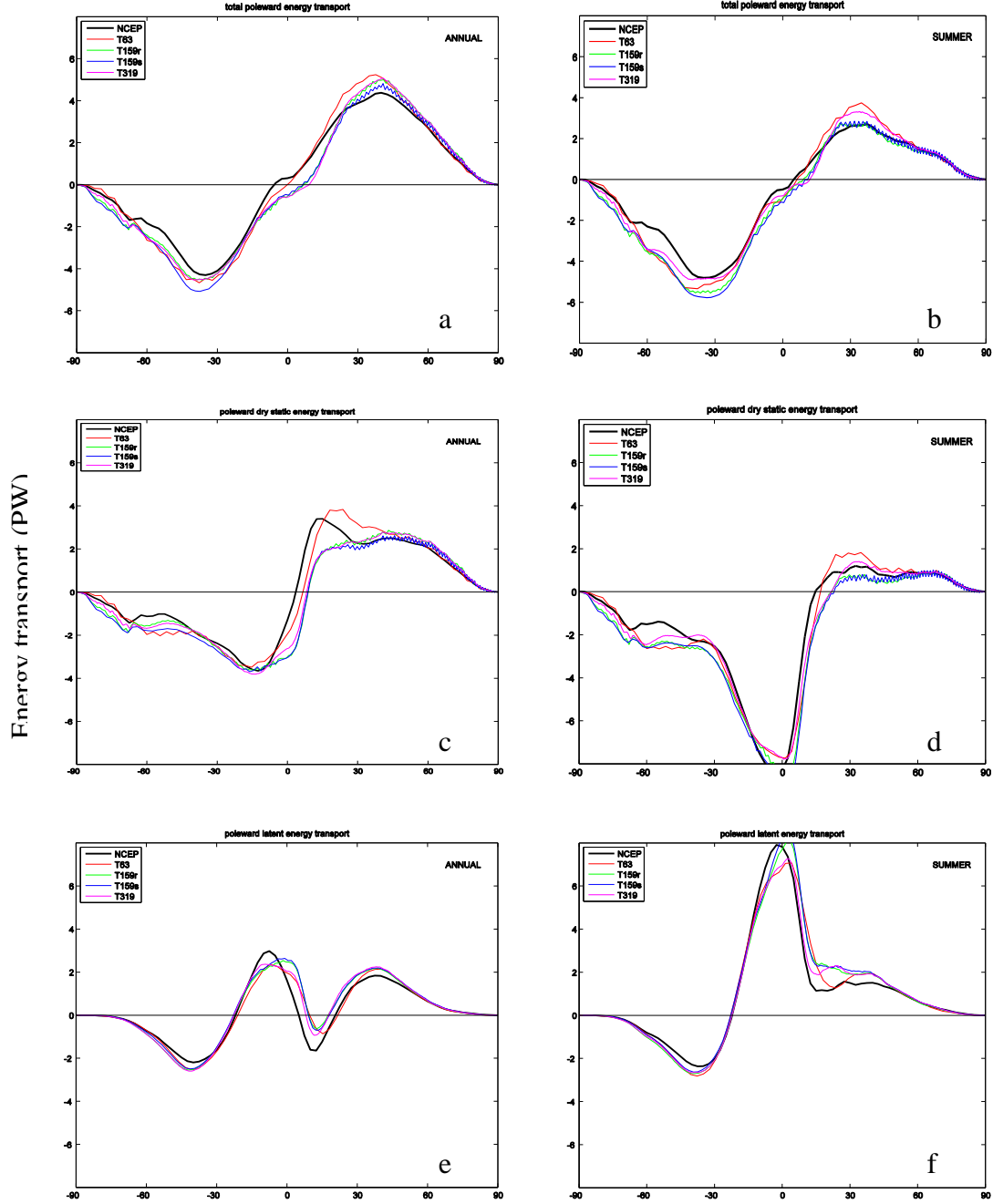


Figure 1. Annual mean (left) and summer (right) for 1979-1990 of the zonal mean poleward atmospheric energy transport in PW. Total energy transport (top), dry static energy transport (middle), latent energy transport (bottom).

Trenberth (1981) noted that mean surface geopotential heights are smaller than the geometric height by 0.1 m in the northern hemisphere, but larger by 0.1 m in the south hemisphere.

4. Results

Better resolution in our experiments gives a more accurate topography and might reduce systematic errors. Here results on the poleward energy transport are presented for the four model experiments and observations.

4.1 The zonal mean poleward atmospheric energy transport

Figure 1 presents the poleward total energy transport T_E for annual mean and summer (June-July-August) season from 1979 to 1990. The total energy transport (Fig. 1 top) is divided into dry static energy transport (Fig. 1 middle) which is the sum of internal energy transport and potential energy transport, kinetic energy transport (small magnitude, not showed) and latent energy transport (Fig. 1 bottom). The annual mean total energy transport is symmetric about the equator with two peaks of 4.8 PW and 4.3 PW around 40°N and 40°S respectively (Fig. 1a). This implies that a flux divergence takes place around those latitudes. The annual mean total energy transport in the four model experiments is in remarkably good agreement with the observations, with maximum transport at the same latitudes. With respect to the maximum transport regions between 30°N and 60°N, it seems that the total energy transport in the higher resolution experiments is closer to the observations than the lower resolution experiment T63. Moreover, the energy transport in experiment T159s is closest to observations at this latitude band. However, the energy transport in experiment T319 is best coherent with observations at the maxima value region from 20°S to 90°S, while there is largest discrepancy at this region in the T159s experiment due to the coarse grid over southern hemisphere. Around equator, it seems that the annual mean total energy transport in the T63 experiment is closest to observation.

Compared with the annual mean energy transport, the poleward total energy transport in summer is, as expected, weaker in northern hemisphere and stronger in southern hemisphere (Fig. 1b). In all the experiments the poleward energy transport is now similarly coherent in tropics. This is because the transport of total energy is less affected by differences in the strength of the Hadley cell due to the near cancellation of the low-level transport of latent and sensible heat to the summer hemisphere (Fig. 1d and 1f). The poleward total energy transport in the T159s and T319 experiments is best coherent with observation in northern and southern extratropics respectively.

The annual mean dry static energy propagates from equator to both the poles respectively (Fig. 1c), while dry static energy in summer transports southwards from 20°N (Fig. 1d). The annual mean latent heat transport appears as a poleward transport at mid-latitudes (Fig. 1e) and in summer as a southward transport at low latitudes (Fig. 1f). Both dry static energy and latent energy transport in the highest resolution experiment are in best agreement with observations in extratropics.

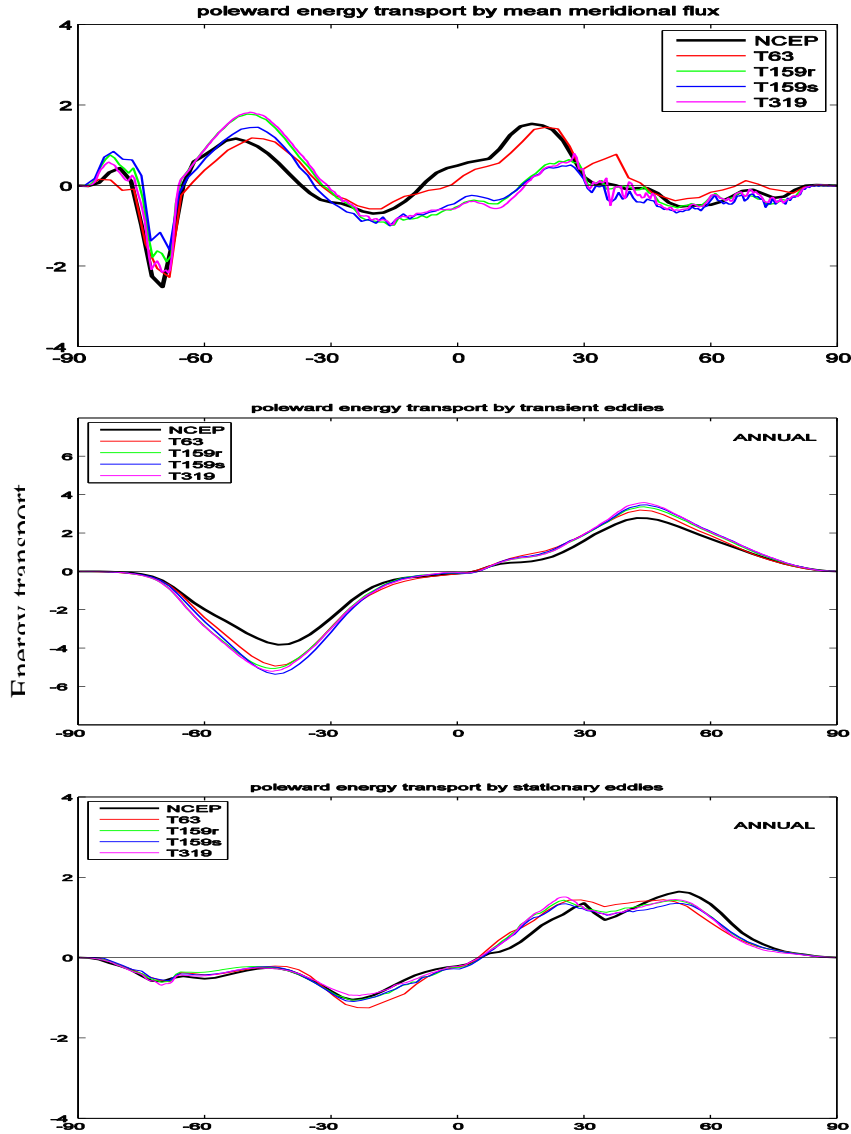


Figure 2. The annual and zonal mean for 1979-1990 of poleward atmospheric energy transport in PW; total energy transport by mean meridional flux (top), total energy transport by transient eddies (middle) and total energy transport by stationary eddies (bottom).

Figure 2 shows component contributions from the transient eddies, stationary eddies and mean meridional circulation to poleward energy transport from 1979 to 1990. The motion of mean flow in the tropics is attributed to the mean vertical overturning in the atmosphere, i.e. the Hadley cell and monsoonal contributions which are dominant in this region. In extratropics baroclinic eddies (cyclones and anticyclones and associated cold and warm fronts) and quasi-stationary planetary waves (e.g. Aleutian Low, Siberian High, Icelandic Low) are active. In tropics the annual mean energy transport contributed by the mean meridional circulation shows best consistency with observations for the coarse resolution experiment T63 (Fig. 2 top), which is similar to what was found in Fig. 1a. This is mainly because the large-scale overturning in tropics, determined by the global monsoon and its embedded Hadley and Walker circulations, could be simulated well with

a low resolution model. It is interesting to see that the energy transport in the T319 experiment shows best consistency with observations at mid-latitudes. Transient eddies are prevalent in the mid-latitude westerlies, where they are generated by baroclinic instability. It is obvious that transport by transient eddies in all experiments are in overall agreement with observations (Fig. 2 middle). The maximum transient transport takes place around 45°N and 45°S in both experiments and observations. However, it seems that transient eddies energy transport in the T63 experiment is closer to observations than the others. This means that higher resolution experiments simulate stronger baroclinic activity and westerlies in mid-latitudes than the lower resolution experiment.

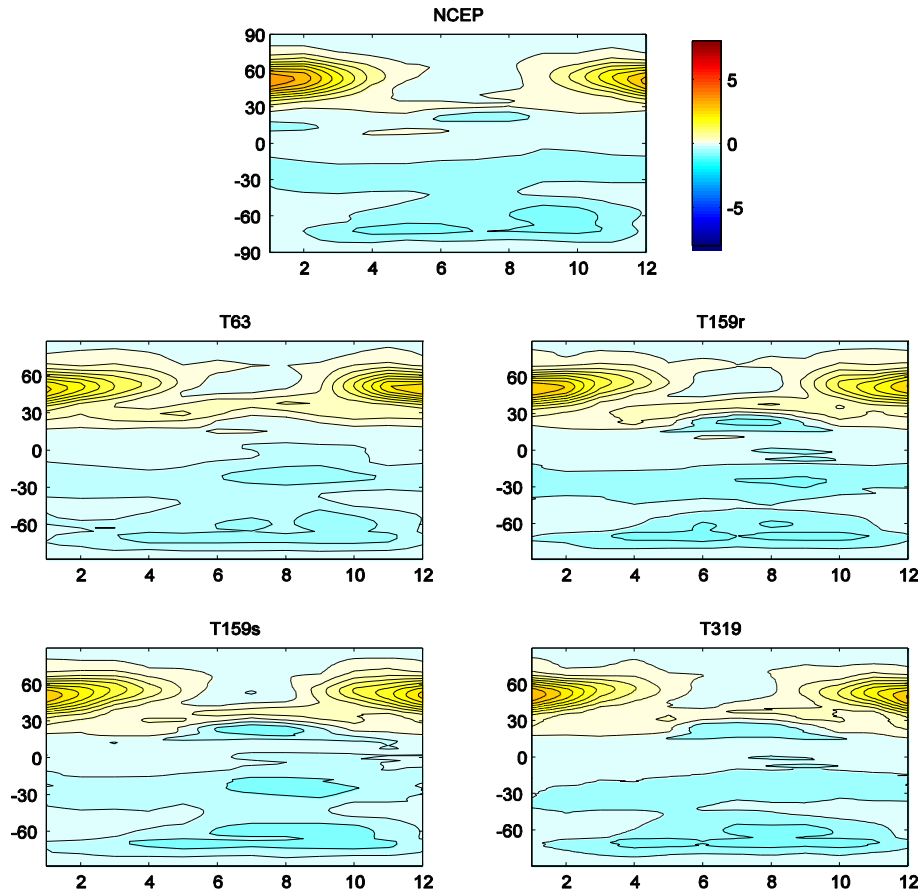


Figure 3. Yearly variation of the dry static energy transport by stationary eddies, unit: PW.

The stationary eddies play an important role in the energy transport in northern mid- and high latitudes (Fig. 2 bottom). The maximum transport takes place around 60°N , which is consistent with the result of Masuda (1988). Better agreement with observations exists in the higher resolution experiments than in the lower resolution experiment. In order to clarify, see the annual variation of stationary eddies energy transport in Figure 3, here the long-term mean monthly dry static energy transport by stationary eddies is presented. Energy transport by stationary eddies is prevalent at mid- and high latitudes in winter in the northern hemisphere. A resolution increase, experiments T319, T159s, T159, shows a better shape and amplitude than that in the T63 experiment compared with the observed

variation. This implies that the increased model resolution exerts a more positive influence for stationary eddies energy transport than for transient eddies energy transport.

4.2 Variability of energy transport

Figure 4a presents the time series of total northward energy transport in northern hemisphere. Note that NCEP data is from 1979 to 2005, while the model experiments are from 1979 to 1990, except for the T319 experiment which ended in 1988. The amplitude of energy transport in the T319 and T159 experiments are closer to observations than in the T159s experiment, while the T63 experiment transmits much more energy towards north. There is a declining trend of total energy transport in the northern hemisphere in the observations, while it is hard to see any similar decreasing trend in the experiments. This is probably due to the short integration periods.

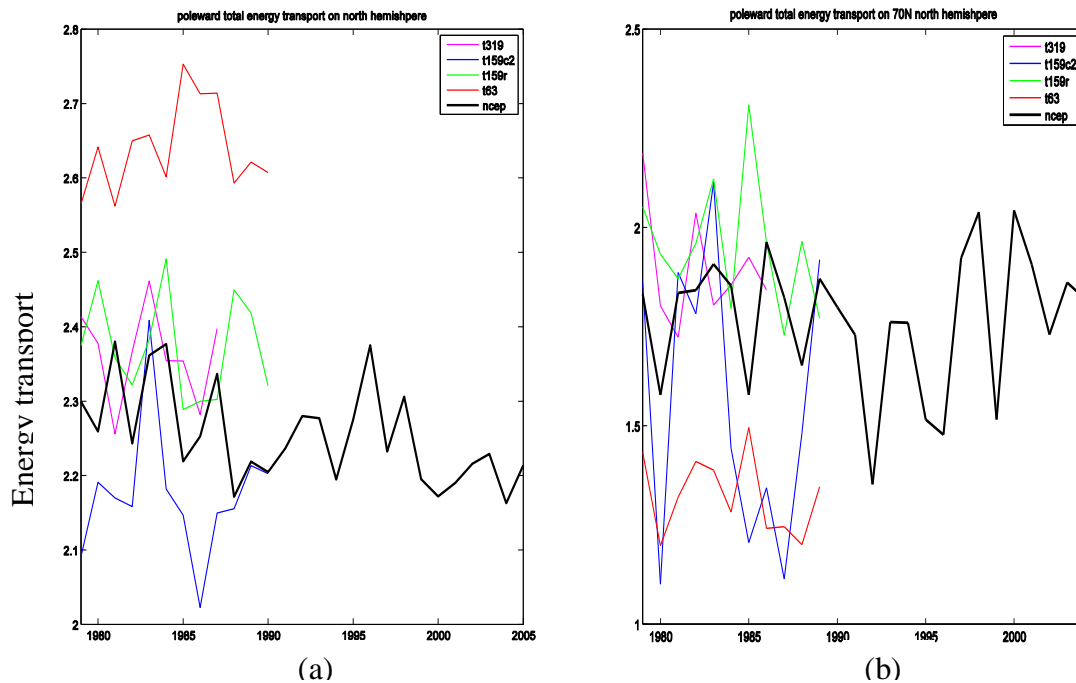


Figure 4. Time series of the total energy transport on the northern hemisphere (a), at 70N (b). NCEP from 1979-2005, T63, T159, T159S from 1979-1990, T319 from 1979-1988. Unit: PW.

The Arctic region is important for global climate. Studies indicate that the interannual and decadal climate variability has a maximum at high latitudes (Räsänen, 2002; Johannessen et al., 2004; Bengtsson et al., 2004; Sorteberg and Kvamstø 2003). However, the climate in high latitudes is complex due to numerous nonlinear interactions between and within the atmosphere, cryosphere, ocean, and land. Sea ice plays a crucial role in the Arctic climate through the albedo-temperature feedback and feedbacks associated with the heat flux through the ice and with clouds. Figure 4b depicts the time series of total poleward energy transport across the latitude at 70°N in winter (DJF). The total energy transported into Arctic in the higher resolution experiments is closer to observations from 1979 to 1988. The T63 experiment transmits less energy into Arctic than the higher resolution experiments and observations. This is opposite to the situation in the T63 experiment for the total transport (Figure 4a). There is no declining trend in northward energy transport across 70°N latitude during this period. However, observations show a rising trend since 1990's which might be associated with the decreasing sea ice cover during the last 15 years (a press release from the National Snow and Ice Data Center, 2006).

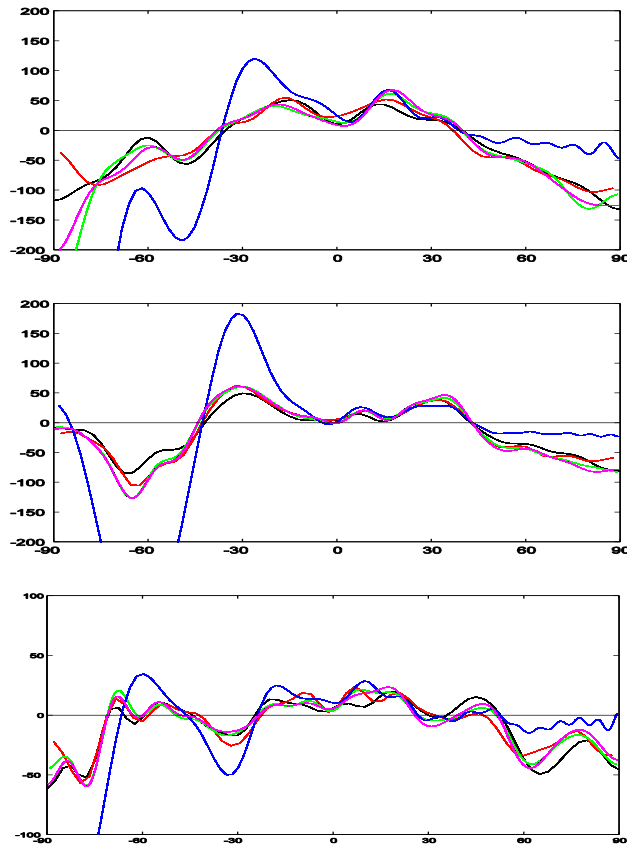


Figure 5. Divergence of the annual and zonal mean for 1979-1990 of total atmospheric energy transport (top), divergence of total energy transport by transient eddies (middle), divergence of total energy transport by stationary eddies (bottom). Unit: WM^{-2} . The legend is same as in Fig.1, Fig2, and Fig.4.

4.3 Divergences of Energy and net upward surface flux

At low latitudes, estimates of atmospheric divergence and the associated large-scale overturning in the Hadley and Walker circulations were especially poor in earlier rawinsonde-based analyses, but have been improving steadily in global numerical analyses based on data assimilation. The divergence of the atmospheric transports varies roughly like a cosine curve with latitude (Fig. 5 top), but with a distinct minimum near the equator which is associated with cold tongue in SSTs, especially in the Pacific (Trenberth and Stepaniak, 2003). The divergence of total energy transport shows positive values between 40°N to 40°S and negative values beyond 40° in each hemisphere. This indicates that mean total energy is transported polewards from low latitudes. It is evident that the divergence in the T319 and T159 experiments agrees well with observations and a little better than in the T63 experiment which also shows too large values near both poles. It is noted that the divergence of total energy transport in the T159s experiment is in the worst agreement with observations at mid- and high latitudes, especially on the southern hemisphere, where it is probably a result from the coarse resolution. It might give a hint how to tune the stretching factor of the model in the T159s experiment. We find the similar disagreement in the T159s experiment for both stationary and transient energy transport (Fig. 5 middle and bottom). The higher the resolution of the model, the better agreement with observations both for stationary and transient energy transport. It is also noteworthy that the zone, where the quasi-stationary component of the energy transport is negative, is almost corresponding to the zone where the transient component is positive. In this way the total energy seems to appear so featureless and produce relatively seamless poleward transports. The transient component of energy transport has largest convergence in the region near 65°S and a largest divergence region around 30°S and 30°N. The stationary component of energy transport shows convergence near 75°S and 65°N. Higher resolution experiments still have better coherence in the stationary case. In order to identify the spatial distribution of the total energy transport in all experiments and compare them with observations, we smooth the transport with a T21 spectral truncation. Figure 6a shows the divergence of total energy transport by transient eddies with T21 spectral truncation for the period (January 1979 – December 1990). The difference between the divergence of total energy transport by transient eddies between experiments and the observations is depicted in Figure 6b. The energy transmission by cyclone eddies is well represented in all the model experiments (Figure 6a). However, all model experiments have larger amplitudes compared with the NCEP data, and there is a too strong amplitude in the southern hemisphere in the T159s experiment due to its coarse resolution over this area. The divergence zones connected to the Aleutian and Icelandic lows and up the Norwegian Sea in the observations are only showed in higher the resolution experiments T159, T159s and T319. This indicates that increased resolution in the model does improve regional phenomena, and thus reflects the main idea of dynamical downscaling.

The above analysis is mostly based on calculations from basic atmospheric variables, now we will show directly the model flux outputs at the surface. In this way, we can compare the surface energy fluxes computed by the physical parameterization in AGCMs with the above calculation. A weakness in the evaluation of the surface fluxes in models comes from the net radiative flux, a source of error in the surface heat budget which can

be found in empirical formulas of radiation, computed explicitly in AGCMs. Now we can use the following method to get a more accurate net surface flux.

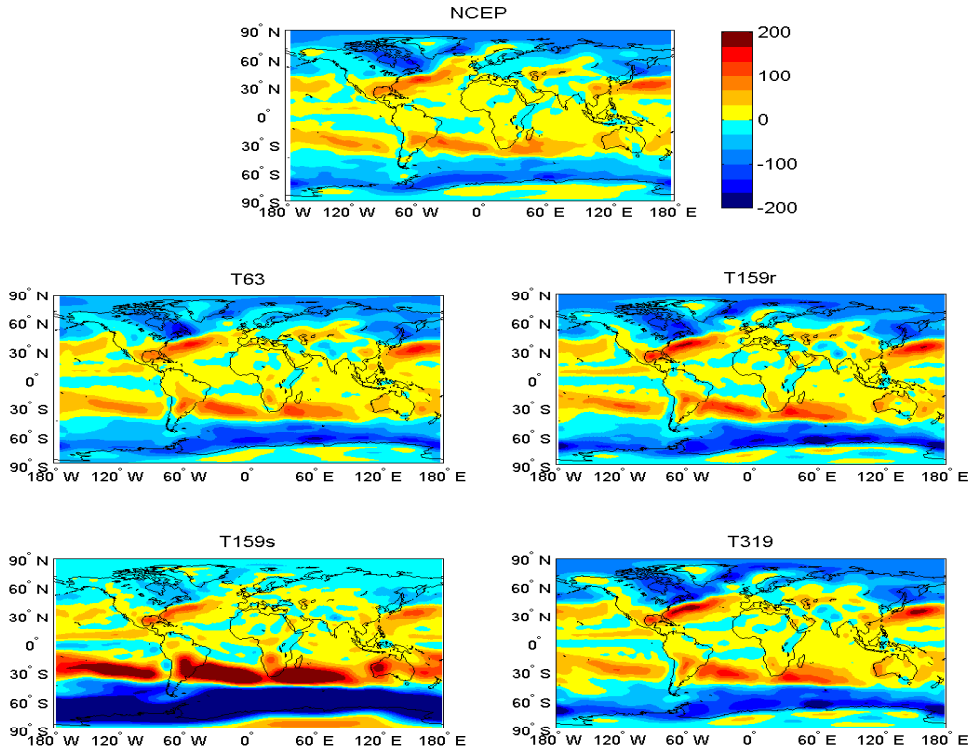


Figure 6a. Divergence of total energy transport by transient eddies at T21 spectral truncation, unit: Wm^{-2} .

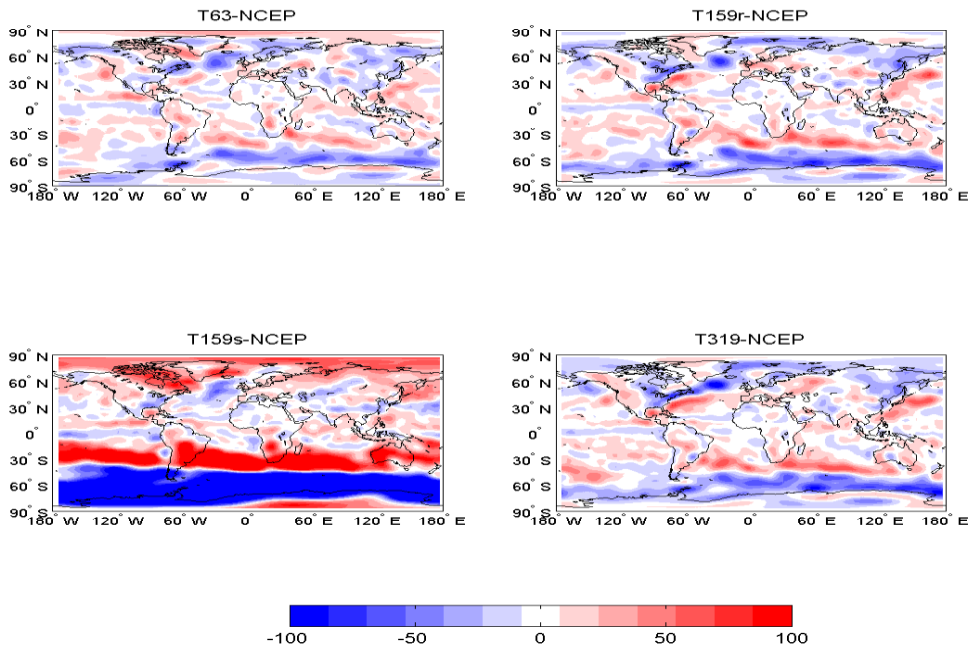


Figure 6b. Difference between models and NCEP of the divergence of total energy transport by transient eddies, unit: Wm^{-2} .

From equation (6) the net upward surface flux F_s can be described as:

$$F_s = \frac{\partial}{\partial t} T_E + \nabla \cdot F_A - R_T$$

where R_T is the net downward radiation through the top-of-the-atmosphere (TOA), and T_E is total energy and F_A is the total energy transport. Figure 7 shows the annual mean net upward surface flux F_s for the period (January 1979 – December 1990) at T31 spectral truncation. Note that we have masked land areas in this figure ideally. F_s should be roughly zero over land areas for times longer than a few months because of its low heat capacity. This can be clearly seen in the figure without masked land areas (not shown). Negative (blue) regions over equatorial and tropical oceans represent a net flux of energy from the atmosphere into the oceans on an annual mean basis, and vice versa. The figure clearly shows the significant net fluxes of energy from the Kuroshio, the Gulf Stream, and the Aghulas Current to the atmosphere. In the T63 experiment the extent and amplitude of F_s is smaller than in the observations. For example, the positive anomaly appears in tropics over the Atlantic Ocean. An increase of resolution to T159, T159s and T319 improves the extent and amplitude of F_s .

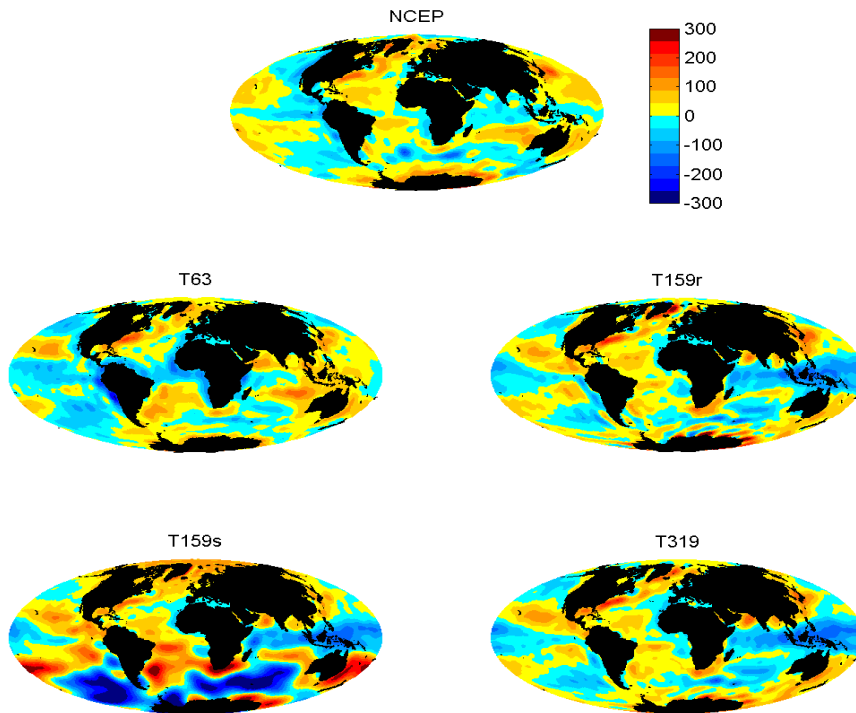


Figure 7. Net upward surface flux F_s in Wm^{-2} at T31 spectral truncation.

4.4 Energy transport in North Atlantic Oscillation events

The North Atlantic Oscillation (NAO) is one of the most prominent and recurrent pattern of atmospheric circulation variability (Hurrell and Kushnir, 2003), it is also a fundamental structure of north hemisphere climate variability (Thompson and Wallace,

1988, 2000). Generally the NAO pattern can be represented by the first EOF of the winter (December-March) mean sea level pressure over northern hemisphere (20°-90°), which explain more than one third of total variance in sea level pressure (SLP), even up to 50% percentage of total variance in SLP in our climate model experiments. We know NAO dictates climate variability from Arctic to the subtropical Atlantic over the northern hemisphere. We will compute the difference in energy transport between the NAO positive phase and the negative phase and estimate how the components of total energy transport contributes to this kind of difference; in other words, how the dry static energy transport, latent energy transport and kinetic energy transport or mean meridional, transient eddies and stationary eddies vary from a positive NAO phase to a negative NAO phase. Understanding the processes that govern the variability in NAO is of high priority, especially in the context of global climate change.

The NAO is the only teleconnection pattern evident throughout the year in the northern hemisphere (Barnston and Livezey, 1987), however, the largest amplitude anomalies in SLP occur during the winter months. We use the EOF (or principal component) method to identify the NAO pattern from the leading eigenvectors of the cross-covariance matrix of winter (DJFM) month SLP. In our experiments, positive NAO events with NAO index > 1.0 and negative NAO events with NAO index < -1.0 are selected. The energy transport based on NCEP data in NAO positive and negative events in the winter months (DJFM) from 1979 to 1991 are showed in Figure 8. The total energy transport in positive NAO events has a similar shape as in negative NAO events, but the amplitude is a bit lower in positive NAO events. In northern hemisphere the total energy in positive NAO events are transported more poleward at 15°N-35°N latitudes and less at 40°N-80°N latitudes than in negative NAO events in winter (Figure 8a). This is because the Iceland Low transmits more energy southward from Arctic and high pressure systems over Atlantic transmit more energy northward in positive NAO events. The Ferrel cells could then be stronger and actually transport more energy from high latitude (cold regions) to low latitude (warm regions). From Figure 8 it is noted that the atmospheric circulation anomaly in the southern hemisphere also affects the NAO teleconnection, although it is a fundamental structure of the northern hemisphere climate variability. In Figure 8b, 8c the variability of dry static energy transport in tropics counteracts the variability of latent energy transport, but it contributes most to the energy transport at 15°N-35°N latitudes and less at 40°N-80°N latitudes. The magnitude of kinetic energy transport is small (10^{14} W), but there is a relative larger amount of kinetic energy transported northward at mid- and high latitudes during the positive NAO events (Figure 8d). From Figure 8e to 8g is shown that mean meridional flux and stationary eddies transports less energy at mid- and high latitudes, which means that the Ferrel cell and the pole eddies transmit more energy from north to south. The transient eddies transport more energy northward over the northern hemisphere in positive NAO events, which is consistent with more cyclone activity during positive NAO events.

The total energy transports in winter (DJFM) based on the results of the four model experiments, in cases when the NAO index exceeds one standard deviation from 1979 to 1991, are depicted in Figure 9. The years of model experiments in positive and negative NAO events are not the same as in NCEP, and there might also be some difference between the model experiments. None of the model experiments are consistent with the NCEP results. To a certain extent the experiment T159R has the best coherence with

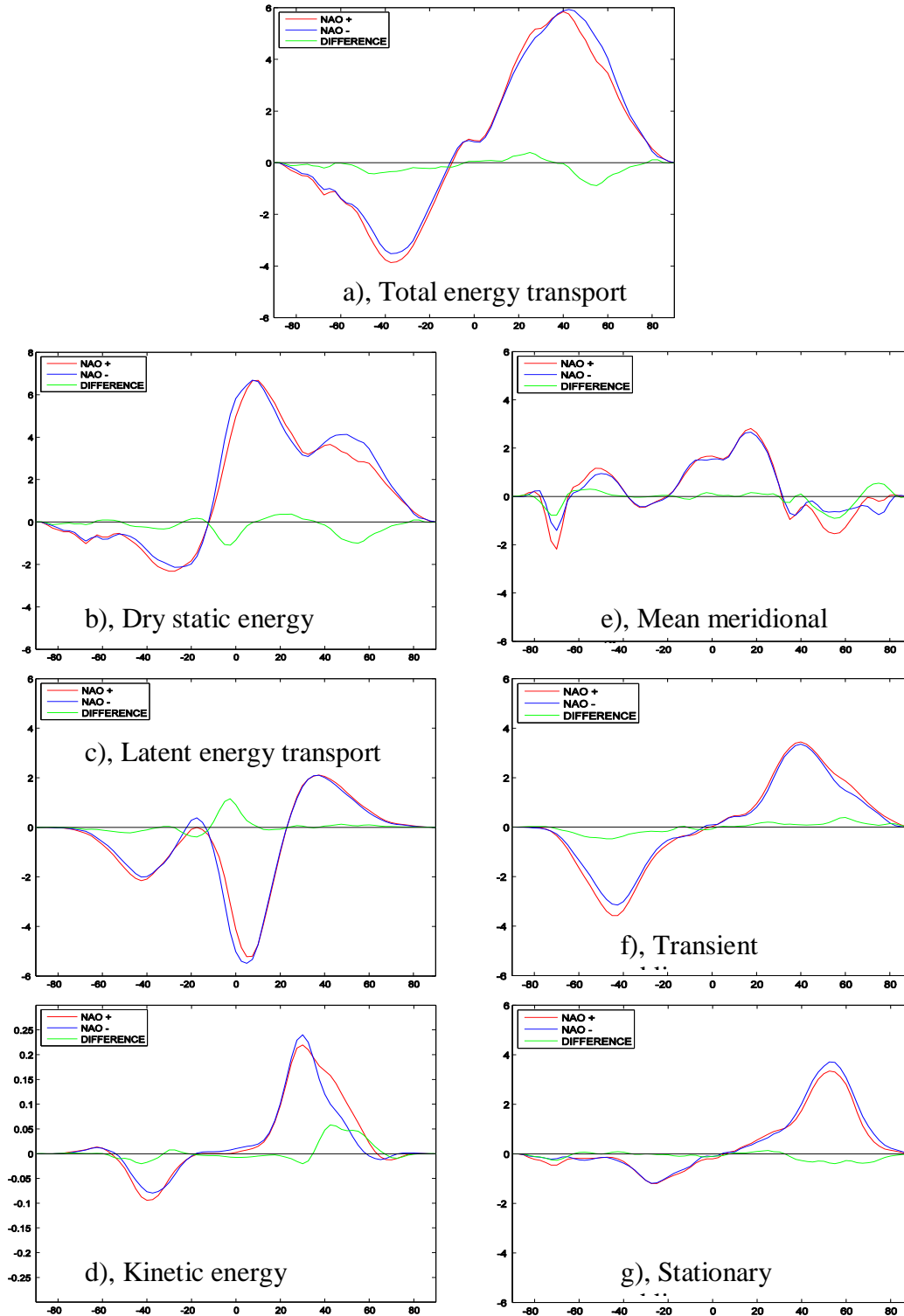
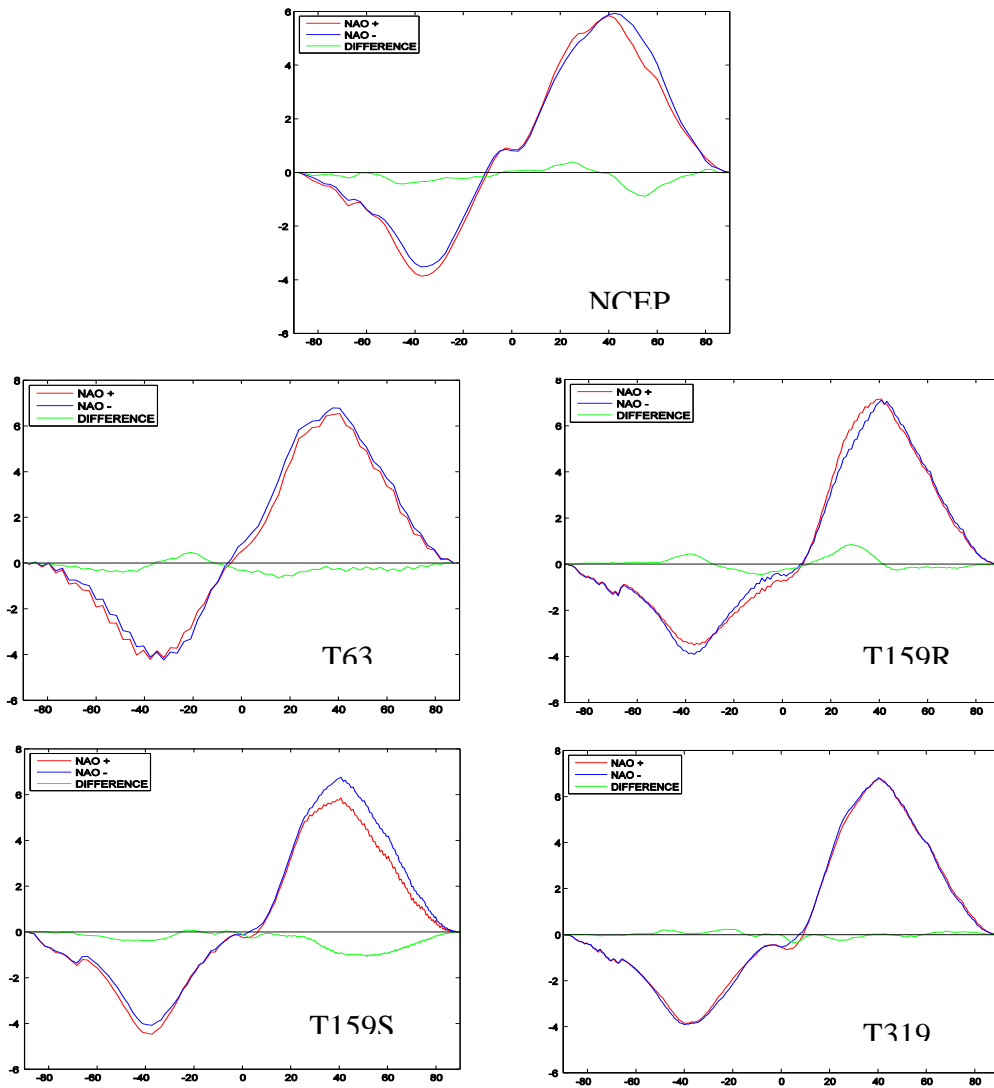


Figure 8, Energy transport based on NCEP data in NAO positive and negative phases in winter months (DJFM) with an NAO index >1.0 and with an NAO index <-1.0 from 1979 to 1991. Unit: PW.

NCEP over the northern hemisphere in shape, and the experiment T159S is closer to NCEP at 40°N-80°N latitudes in magnitude. Energy transport in the experiment T319

with highest resolution, changes little between positive and negative NAO events. The probably reason is that the period of the T319 experiment is too short (1979-1988) and the amplitude of it's NAO index is also relatively smaller compared with other model



experiments from their NAO pattern figures (not shown). The T319 experiment need huge computer resources, and it took several months to integrate 10 years.

Figure 9, total energy transport based on NCEP data and four model experiments in winter months (DJFM) with an NAO index >1.0 and with an NAO index <-1.0 from 1979 to 1991. Unit: PW.

Recently, the precipitation impact of NAO over Europe has been quantified using two different approaches: first, the use of raingauge-based, land-only precipitation observations (Hurrell and van Loon, 1997); and second, plots of evaporation minus precipitation ($E - P$), computed as a residual of the atmospheric moisture budget from analysis data sets (Hurrell 1995, Hurrell and van Loon 1997). Despite being closer to 'reality', the first approach is undermined by lack of data over many areas, especially over the oceans. In contrast, the second approach can be applied to both land and oceans.

Evaporation exceeds precipitation over Greenland and the Canadian Arctic during high NAO index winters (NCEP in Figure 10), where changes between high and low NAO index states are on the order of 3 mm day^{-1} . Drier conditions of the same magnitude also occur over much of central and southern Europe, the Mediterranean and parts of the Middle East, whereas more precipitation than normal falls from Iceland through Scandinavia. All the model experiments show same results regarding that the evaporation exceeds precipitation over central and southern Europe, the Mediterranean and parts of the Middle East (the model experiments in Figure 10). The increased precipitation from Iceland to Scandinavia has a better position and a better magnitude in the high resolution experiments T159R and T319. The drier condition over Greenland and the Canadian Arctic is consistent with NCEP data for T319 as well. Changes in the mean flow and storminess associated with swings in the NAO index, are also reflected in pronounced changes in the distribution of evaporation and precipitation, and thus, the transport and convergence of atmospheric moisture. Figure 11 represents the difference of the divergence of latent energy transport between winter months (DJFM) for positive NAO phase and negative NAO phase from 1979 to 1991. This figure shows a very good coherence with Figure 10, the divergence area of latent energy occurs over Greenland and Canadian Arctic, southern Europe, the Mediterranean and parts of the Middle East; the region from Iceland through Scandinavia is a convergence area.

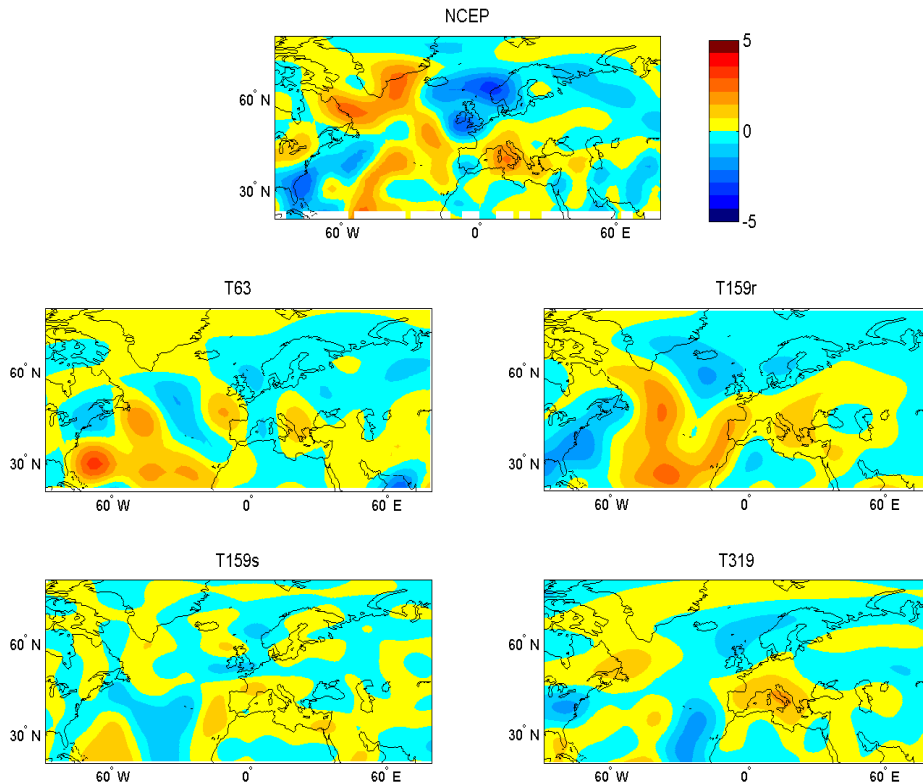


Figure 10, Difference in mean winter evaporation (E) minus precipitation (P) between winter months (DJFM) with an NAO index >1.0 and with an NAO index <-1.0 from 1979 to 1991. Unit: mm/day.

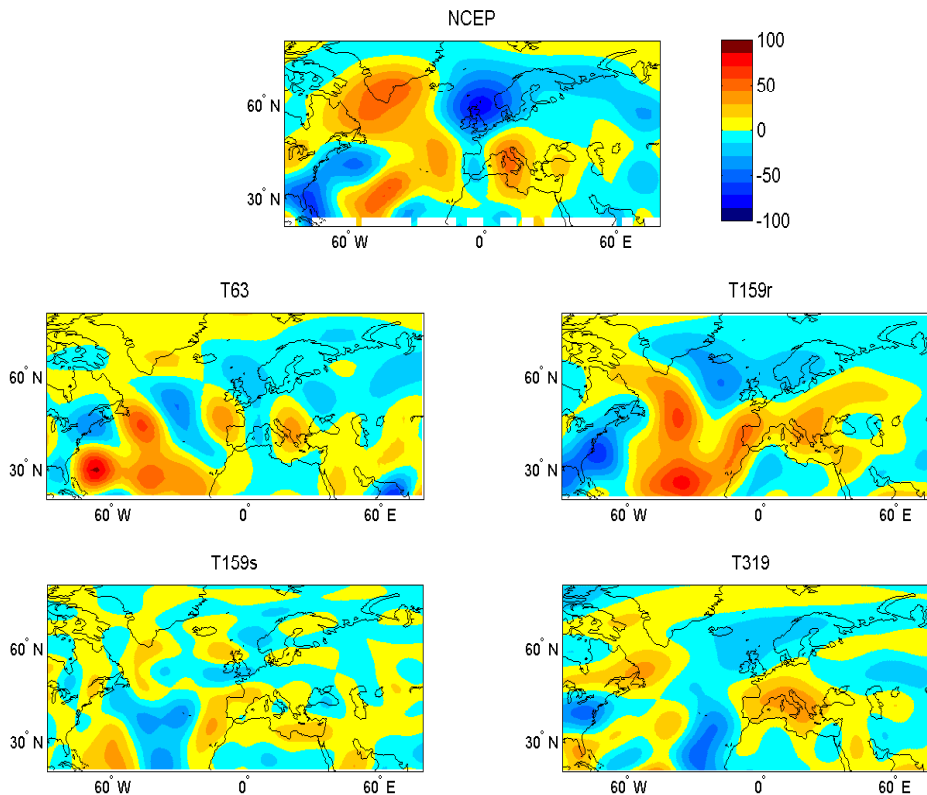


Figure 11, Difference in the divergence of latent energy transport between winter months (DJFM) with an NAO index >1.0 and with an NAO index <-1.0 from 1979 to 1991. Unit: Wm^{-2}

4.5 Downscaling of dry static energy and latent energy transport by transient eddies at the 925mb

The main purpose of downscaling is to simulate the climate of parameters more directly connected to local weather, such as temperature, precipitation and surface wind. We know that even the resolution in T319 is too coarse to describe climate variations in mountainous terrain like that in Norway. Where surface observations exist, empirical downscaling based on the results from dynamical downscaling is possible for estimation of local weather and climate. We will here just demonstrate how the situation of the dry static energy and latent energy transport by transient eddies vary with resolution, concentrating on areas covering the Norwegian and the Barents Sea and surrounding land areas. Dry static energy and latent energy transport by transient eddies at 925mb for an area covering the Norwegian and Barents Sea are presented in Figure 12a and 12b. We have chosen to use this pressure layer instead of 1000 mb which might decrease and neglect the impact of the lower boundary on weather systems due to vortex and turbulence in meso- and small scale system. Moreover, we have chosen 925 hPa mainly because effects of mountain ranges like the Scandinavian mountains will be noticeable. The dry static and latent energy transport by transient eddies has a good coherence compared with observations to the storm track areas from the north Atlantic Ocean to Barents Sea in all experiments. The dry static energy transmitted by transient eddies goes through the passage

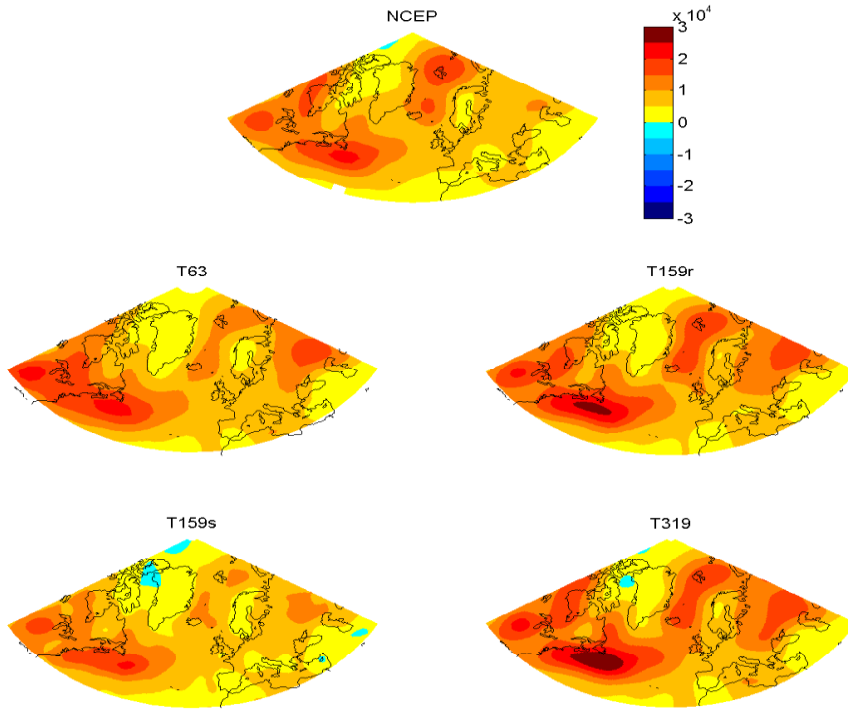


Figure 12a. Annual mean dry static energy by transient eddies at 925 hpa, unit: J.

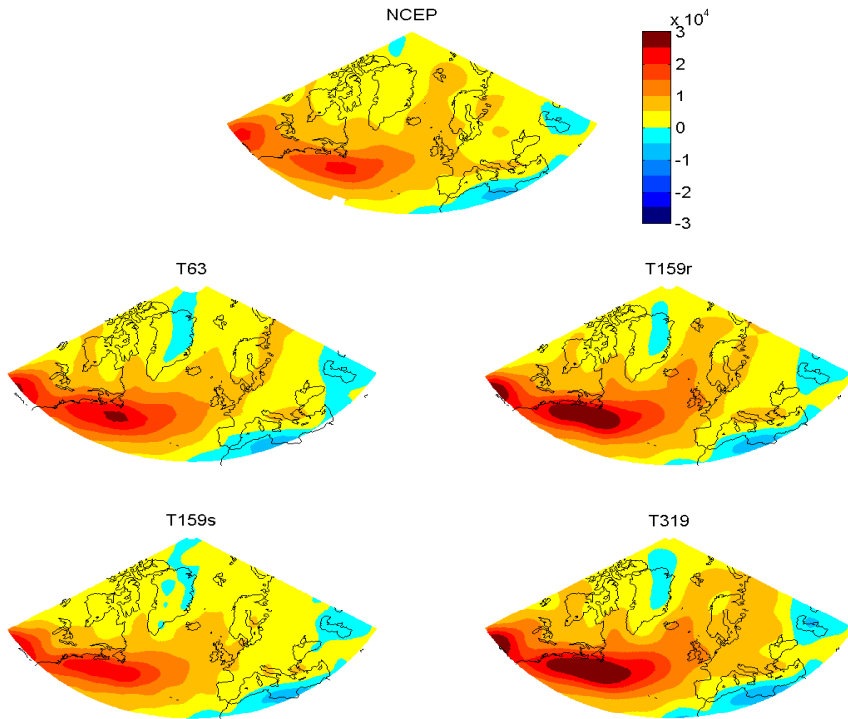


Figure 12b. Annual mean latent energy by transient eddies at 925 hpa, unit:J.

between Greenland and Norway from south of Iceland towards the Barents Sea. This phenomena is best simulated in the highest resolution experiment T319. The magnitude

of simulated energy is less in the T63 and T159s experiments than in the observations, while it is stronger in the T159 experiment. It is clearly seen that in the T319 experiment, some structures are connected to mountains, while these structures are not so clear in the lower resolution experiments. The latent energy transport by transient eddies can reach the Barents Sea in the experiments (as in observations), except for the T63 experiment. The latent energy can bring more moist air and precipitation in the area south of Iceland and also up to the eastern part of the Norwegian Sea. This increase illustrates both an effect of changes in the storm tracks and stronger vertical circulation with increased resolution (this is described in another paper).

5. Concluding remarks

Atmospheric modeling provides an opportunity to reveal the mechanisms of heat transport. Knowledge of observed meridional energy transport in the atmosphere can also be used in the evaluation of AGCMs. It is vital to represent the energy variation and keep energy conservation well in the AGCMs.

The poleward total energy transport in high resolution experiments shows a better agreement with NCEP reanalysis data at mid- and high northern latitudes than in the low resolution experiment. This is also found for poleward dry static energy transport and latent heat transport components. In tropics, however, the poleward total energy transport in the low resolution experiment is closer to NCEP data. The same is found for poleward dry static energy transport and latent heat transport components.

The energy transport by stationary eddies in higher resolution experiments has a better agreements with NCEP data than the low resolution experiment T63. There are, however, higher amplitudes of energy transport by transient eddies in higher resolution experiments due to stronger simulation of baroclinic activity at mid-latitudes.

The time series variability of total northward energy transport on the northern hemisphere is better represented in higher resolution experiments than in the T63 experiment. There is a declining trend of total energy transport over northern hemisphere in the NCEP data. It is, however, hard to state that there is less and less energy transported poleward. Hence a longer time series period is needed to make the trend meaningful for global warming. The energy transported into Arctic in higher resolution experiments is closer to NCEP data, the T63 experiment transmits much less energy into Arctic. This is opposite to the situation of T63 above. In the observations there is a rising trend of northward energy transport at 70°N latitude from 1991.

The influence of model resolution on the divergence of energy transport, which represents the source and convergence of energy, is the same as in the results above. The net surface flux over the Atlantic is better represented by the high resolution experiments both in extent and strength. The detailed information for local areas, such as Norway, can only be provided by the highest resolution experiment T319.

During positive NAO events, the energy transported poleward is less at low latitudes, but stronger at mid- and high latitudes of the northern hemisphere compared with the energy transported poleward during negative NAO events. The largest contribution comes from dry static energy transport and stationary energy transport. As for the precipitation impact of NAO over Europe, the distribution of evaporation and precipitation is exactly consistent with the transport and convergence of atmospheric moisture.

Increased horizontal resolution benefits the calculation of the energy transport, but improved vertical resolution is probably also important. In particular, improved vertical resolution is needed in the boundary layer for the moisture budget, and in the boundary layer and upper troposphere for calculation of divergence. In this study all model experiments had the same vertical resolution (31 levels). According to Trenberth and Stepaniak (2002) this is not enough to calculate accurate atmospheric energy budgets. Low vertical resolution could be one reason that higher horizontal resolution experiments not always improves the simulation of energy transport. In future work the model experiments with different vertical resolution should be considered as well.

Acknowledgments. This investigation was supported by Research Council of Norway through MACESIZ project. We thank Prof. Sigbjørn Grønås for helpful comments and suggestions.

REFERENCES

- Barnston, A. G., and R. E. Livezey, Classification, seasonality and persistence of low frequency atmospheric circulation patterns, *Mon. Wea. Rev.*, 115, 1083–1126, 1987.
- Bengtsson, L. and J. Shukla, 1988: Integration of space and in situ observations to study global climate change. *Bull. Amer. Meteor. Soc.* 69, 1130-1143.
- Boer, G. J. 1986: A comparison of mass and energy budgets from two FGGE datasets and a GCM. *Mon. Wea. Rev.* 114, 885-902.
- Bromwich D. H. and S. Wang, 2005: Evaluation of the NCEP–NCAR and ECMWF 15- and 40-Yr Reanalyses Using Rawinsonde Data from Two Independent Arctic Field Experiments. *Mon. Wea. Rev.* 133, 3562–3578.
- Carissimo, B. C., A. H. Oort and T. H. Vonder Haar, 1985: Estimating the meridional energy transport in the atmosphere and the ocean. *J. Phys. Oceanogr.* 15, 82-91.
- Courtier, P. and J.-F. Gelayn, 1988: A global numerical weather prediction model with variable resolution: Application to the shallow- water equations. *Quart. J. Roy. Meteor. Soc.*, 114, 1321–1346.
- Dickson, R. R., T. J. Osborn, J. W. Hurrell, J. Meincke, J. Blindheim, B. Adlandsvik, T. Vigne, G. Alekseev, and W. Maslowski, The Arctic Ocean response to the North Atlantic Oscillation, *J. Climate*, 13, 2671–2696, 2000.
- Deque, M., and J. P. Piedelievre, 1995: High resolution climate simulation over Europe. *Climate Dyn.*, 11, 321–339.
- Fortelius, C. and E. Holopainen, 1990: Comparison of energy source estimates derived from atmospheric circulation data against satellite measurements of net radiation. *J. Climate* 3, 646-660.
- Fox-Rabinovitz M. S. , L. L. Takacs, R. C. Govindaraju and M. J. Suarez. 2001: A Variable-Resolution Stretched-Grid General Circulation Model: Regional Climate Simulation. *Mon. Wea. Rev.* 129, 453–469.
- Giorgi, F. and L. O. Mearns, 1999: Introduction to special section: regional climate modeling revisited. *J. Geophys. Res.* 104, 6335–6352.
- Gruber, A. 1970: The energy budget over the Florida Peninsula when a convective regime dominates. *J. Appl. Meteor.* 9, 401-416.
- Hurrell, J. W., Decadal trends in the North Atlantic oscillation: Regional temperatures and precipitation, *Science*, 269, 676–679, 1995a.

- Hurrell JW, van Loon H (1997) Decadal variations in climate associated with the North Atlantic Oscillation. *Clim Change* 36:301–326.
- Hastenrath, S. 1982: On meridional heat transport in the world ocean. *J. Phys. Oceanogr.* 12, 922-927.
- Holloway G. and T. Sou, 2002: Has Arctic sea ice rapidly thinned? *J. Climate* 15, 1691-1701.
- Holopainen, E. and C. Fortelius, 1986: Accuracy of estimates of atmospheric large-scale energy flux divergence. *Mon. Wea. Rev.* 114, 1910-1921.
- Masuda, K. 1988: Meridional heat transport by the atmosphere and the ocean. *Tellus*, 40A, 285-302.
- Murphy J. 1999: An Evaluation of Statistical and Dynamical Techniques for Downscaling Local Climate. *J. Clim.* 12, 8, 2256–2284.
- Kann, D. M., S. Yang and A. J. Miller, 1994: Mean meridional transport of energy in the earth-atmosphere system using NMC global analyses and ERBE radiation data. *Tellus*, 46A, 553-565.
- Keith, D. W., 1995: Meridional energy transport: uncertainty in zonal means. *Tellus*, 47A, 30-44.
- Masuda, K. 1988: Meridional heat transport by the atmosphere and the ocean. *Tellus*, 40A, 285-302.
- McGregor, J. L. 1997: Regional climate modeling. *Meteorol. Atmos. Phys.* 63, 105–117.
- Michaud, R. and J. Derome, 1991: On the mean meridional transport of energy in the atmosphere and oceans as derived from six years of ECMWF analyses. *Tellus*, 43A, 1-14.
- Moritz R. E., C. M. Bitz and E. J. Steig, 2002: Dynamics of recent climate change in the Arctic. *Science* 297, 1497-1502.
- Oort, A. H. and J. P. Peixóto, 1983: Global angular momentum and energy balance requirements from observations. *Adv. Geophys.* 25, 355-490.
- Piexoto, J. P., and A. H. Oort, 1992: *Physics of Climate*. New York, American Institute of Physics, 520 pp.
- Reynolds, R. W. and T. M. Smith, 1994: Improved global sea surface temperature analyses using optimum interpolation. *J. Clim.*, 7, 929-948.
- Sardeshmukh, P. D. and B. J. Hoskins, 1984: Spatial smoothing on the sphere. *Month. Wea. Rev.*, 112, 2524 -2529.
- Schmidt, F., 1977: Variable fine mesh in a spectral global model. *Beitr. Phys. Atmos*, 50, 211–217.
- Simmons, A. J., and J. K. Gibson, 2000: The ERA-40 project plan. ECMWF ERA-40 Project Report Series 1, ECMWF (Available online at <http://www.ecmwf.int/publications/library/do/references/list/192>).
- Thompson, D. W. J., and J. M. Wallace, The Arctic Oscillation signature in the wintertime geopotential height and temperature fields, *Geophys. Res. Lett.*, 25, 1297–1300, 1998.
- Thompson, D. W. J., and J. M. Wallace, Annular modes in the extratropical circulation, Part I: Month-to-month variability, *J. Climate*, 13, 1000–1016, 2000.
- Thompson, D. W. J., J. M. Wallace, and G. C. Hegerl, Annular modes in the extratropical circulation, Part II: Trends, *J. Climate*, 13, 1018–1036, 2000.

- Trenberth, K. E., 1991: Climate diagnostics from global analyses: Conservation of mass in ECMWF analyses. *J. Climate*, **4**, 707–722.
- Trenberth, K. E., 1995: Truncation and use of model-coordinate data. *Tellus*, **47A**, 287–303.
- Trenberth, K. E., 1997: Using atmospheric budgets as a constraint on surface fluxes. *J. Climate*, **10**, 2796–2809.
- Trenberth, K. E., and A. Solomon, 1993: Implications of global atmospheric spatial spectra for processing and displaying data. *J. Climate*, **6**, 531–545.
- Trenberth, K. E., and C. J. Guillemot, 1998: Evaluation of the atmospheric moisture and hydrological cycle in the NCEP/NCAR reanalyses. *ClimateDyn.*, **14**, 213–231.
- Trenberth, K. E., and J. M. Caron, 2001: Estimates of meridional atmosphere and ocean heat transports. *J. Climate*, **14**, 3433–3443.
- Trenberth, K. E., D. P. Stepaniak, and J. M. Caron, 2002a: Accuracy of atmospheric energy budgets. *J. Climate*, **15**, 3343–3360.
- Trenberth, K. E., D. P. Stepaniak, and J. M. Caron, 2002b: Interannual variations in the atmospheric heat budget. *J. Geophys. Res.*, **107**, 4066, doi:10.1029/2000D000297.
- Vonder Haar T. H. and A. H. Oort, 1973: New estimate of annual poleward energy transport by northern hemisphere oceans. *J. Phys. Oceanogr.* **3**, 169-172.
- Wergen, W. 1988: The diabatic ECMWF normal mode initialization scheme. *Beitr. Phys. Atmosph.* **61**, 274-302.